Optimization of a combined thermal annealing and isostatic pressing process for mechanical and surface enhancement of Ultem FDM parts using Doehlert experimental designs

Ariadna Chueca de Bruijn[a], Giovanni Gómez-Gras[a,*], Laura Fernández-Ruano[a], Laia Farràs-Tasias[a], Marco A. Pérez[a]

[a]*IQS School of Engineering, Universitat Ramon Llull, Via Augusta 390, 08017 Barcelona, Spain*

Abstract

The mechanical anisotropy of Fused Deposition Modeling (FDM) fabricated parts due to voids and non-uniform bond formation between rasters represents a major challenge for the widespread adoption of this fabrication technique. The present article addresses a novel post-processing procedure for FDM Ultem™ 9085 parts based on thermal annealing coupled with isostatic pressing to produce specimens with improved mechanical and surface properties. Response surface methodology was used to obtain mathematical models for all the studied responses. In particular, the sequentiality of Doehlert Designs was exploited to select the optimal combination of time and temperature of the process, resulting in specimens with noticeably improved layer adhesion, as noted by enhancements in flexural modulus, flexural strength, strain at flexural strength, and surface roughness. Confirmatory experiences of the optimal point with different printing orientations have demonstrated the capability of the proposed method to reduce anisotropy in the mechanical properties of the treated parts. In addition, microscopy imaging, Raman spectroscopy, and X-ray diffraction were beneficial to justify the observed results. This study sheds new light on the post-processing of FDM polymers, and the presented optimization methodology can be extrapolated to other materials and processes.

Keywords: Additive manufacturing (AM), Fused deposition modeling (FDM), Response surface methodology (RSM), Doehlert Design, Thermal annealing, Ultem 9085

1. Introduction

The layer-by-layer deposition nature of Fused Filament Fabrication (FFF), also known as Fused Deposition Modeling (FDM), offers a broad spectrum of possibilities to manufacture complex-shaped parts that would otherwise be unfeasible using conventional methods. While this filament extrusion-based process was initially conceived for prototype creation, recent technological advancements suggest its potential to produce moderate to mass quantities of end-products and meet individual customer demands more quickly [1].

*Corresponding author.
Email address: giovanni.gomez@iqs.edu (Giovanni Gómez-Gras)

As evidenced in an early study conducted by Bellehumeur et al. [2], the final characteristics of FDM parts in terms of mechanical performance and surface finish are highly influenced by the quality of the bonding between individual polymer filaments. This is a complex phenomenon the modeling of which should also consider the geometry's complexity, thermal boundary conditions, and gravitational loads [3]. In turn, the bond formation depends on the neck growth within adjacent filaments that begin to fuse and on the molecular diffusion at the interface. In this sense, Wang et al. [4] correlated the surface roughness of fused filament fabricated parts with the diffusion among deposited filaments through a predictive numerical model. Molecular diffusion requires sufficient time at high temperatures, which explains the observation made by Morales et al. [5] (who characterized interlayer bonding of FDM specimens through compression tests) that the layer-to-layer bonding strength is weaker than between coplanar filaments, as the polymer has had more time to cool down between successive layers than within the same layer. In another study, Shelton et al. [6] showed that the amount of neck growth improved with increasing envelope temperatures and resulted in parts with higher strengths and improved consistencies.

Therefore, investigating how the selected printing process parameters (air gap, layer height, number of contours, raster angle, build orientation, nozzle design, and extruder and chamber temperatures) affect the bonding is critical to obtain components with optimized performance [7]. For instance, Fountas et al. [8] generated a regression model to examine the influence of five of the aforementioned FDM process input variables on the flexural strength of polyethylene terephthalate glycol (PET-G) components and found the set of optimal conditions that maximized the material's mechanical performance. For their part, Forés-Garriga et al. [9] published an extensive study where multiple infill configurations were considered, and compliance matrices which enabled to determine a correlation between the FDM settings and the mechanical performance of the intra-layer and inter-layer unions were provided.

A review published by Chohan and Singh [10] indicated that an alternative approach which has achieved promising results to reduce the mechanical anisotropy and enhance the surface properties of FDM parts consists of applying thermal, chemical, or mechanical processes following manufacturing. In this sense, Chueca de Bruijn et al. [11] compared the surface characteristics of FDM specimens after application of six post-processing techniques and noticed notable differences in surface roughness as a function of the chosen method.

Among all post-processes, thermal annealing is a well-established technique that uses heat to alter the physical and sometimes chemical properties of a material. The part is usually treated at elevated temperatures and then slowly cooled, which relieves internal stresses introduced during manufacturing. Concerning the FDM process, when a polymeric melt is cooled, the inhomogeneous temperature distribution causes volumetric shrinkage and the generation of residual stresses, which can negatively impact the final performance of the part, as affirmed by Sreejith et al. [12]. With semicrystalline materials such as polylactic acid (PLA), Wach et al. [13] found that thermal annealing above their glass-transition temperature (T_g) results in an increase in the degree of crystallinity of its structure and an enhanced mechanical behavior. Otherwise, in the case of amorphous polymers, the observed phenomenon is a structural relaxation that leads to higher indentation hardness and Young's modulus [14]. In addition, a notable increase in inter-laminar fracture toughness of FDM acrylonitrile butadiene styrene (ABS) parts was demonstrated by Hart et al. [15] after post-manufacture isothermal heating above the material's T_g in a supporting uniaxially compressed fixture, showing the potential of the combined use of temperature and pressure to treat additively manufactured components.

An engineering-grade thermoplastic that continues to attract increasing interest to both the scientific community and the industrial sector is the polyetherimide (PEI) Ultem™ 9085 (henceforth, PEI Ultem) [16–18]. This high-performance material stands out for its strength-to-weight ratio and its flame-retardant, low smoke evolution, and low toxicity (FST rating), which make it a promising candidate to be adopted by the aerospace [19], automotive, and military industries [20]. PEI Ultem's high glass transition temperature (around 180 ◦C) and chemical resistance justify the reduced number of published scientific literature concerning its post-processing. Chueca de Bruijn et al. [21] proposed the use of ball-burnishing to increase the fatigue life and reduce the surface roughness of PEI Ultem parts. Seneviratne et al. [22] applied a metallic coating to PEI Ultem specimens which improved the part's tensile and flexural mechanical performance. McLouth et al. [23] found that atmospheric plasma treatment (APT) could be used to produce an effective strength recovery of damaged tensile dogbone PEI Ultem specimens, which makes APT a valid repair method for damaged 3D-printed structures.

To the authors' knowledge, thermal studies with PEI Ultem have only been performed below its T_g. In one case study presented by Padovano et al. [24], PEI Ultem's mechanical properties were found sensitive to a sudden variation of temperature, but no adverse effects were detected when it was maintained at a high temperature or when its temperature changed gradually. In another work, Zhang et al. [25] thermally treated PEI Ultem specimens with a 24-to −96-hours low-temperature annealing process and observed an expansion in the layering direction, indicating relief of thermal stresses. Moreover, mesostructure and fracture analysis indicated increased ductility and enhanced coalescence without significant geometrical distortion. These results reveal that the use of temperature in the post-processing of FDM parts could have beneficial effects in reducing the inherent shortcomings of the technology itself.

To discern between significant and non-significant changes of a specific process, the use of robust statistical methods is thought to be of utmost importance. Response surface methodology (RSM) is a collection of mathematical and

statistical techniques essentially conceived to optimize independent process variables to obtain the desired responses through a series of experiments [26]. In a sufficiently small volume of the design space, quadratic polynomial models can be used to predict the studied responses. In this sense, there are two main experimental design matrices to adjust quadratic functions: the Central Composite Design (CCD) and the Box–Behnken Design (BBD). Within the field of additive manufacturing, the consulted literature reveals the higher popularity of full-factorial and Taguchi methods (when no quadratic function is required) [27–29] or CCD and BBD (when sophisticated modeling approaches are needed) [30,31]. Nonetheless, despite not being as widely used as the other matrices, Uniform Shell or Doehlert Designs (DD) [32] allow estimation of the terms of the quadratic model with a smaller number of experiments. They also enable the detection of lack of fit in the calculated model as well as the creation of sequential designs. Consequently, depending on the obtained results, the initial experimental matrix can be moved towards a new experimental domain closer to the optimal zone using points from the first matrix [33]. In this context, in one of the few optimization approaches that use DD in additive manufacturing, Ginoux et al. [34] conducted one iteration of a DD to optimize the printing speed and extrusion temperature to build FDM PLA/layered silicate nanocomposite parts and understand the impact of these process parameters on the tensile properties of the material.

The aim of this research is to provide experimental evidence on the benefits of thermal post-treatments of FDM polymers intended to improve the bonding strength between filaments and reduce mechanical anisotropy through densification of the final parts. Accordingly, this work presents a novel high-temperature thermal annealing approach performed in a pressurized environment to post-process FDM PEI Ultem parts. A sequential DD methodology is used to obtain a robust mathematical model to predict changes in the specimens' mechanical performance and surface roughness and optimize the time and temperature of the annealing treatment. Confirmatory experiments using different printing configurations are used to verify the predicted optimal treatment conditions, and the obtained surface and mechanical enhancements are evidenced by microscopy analysis. Potential changes in PEI Ultem's chemical structure after the treatment are investigated using X-ray diffraction and Raman spectroscopy.

2. Methodology

2.1. Design of experiments

A schematic of the methodology followed in the present work is shown in Fig. 12 in Appendix. Considering the possibility of extending the initial experimental domain, a Doehlert Design was chosen to perform the initial design of experiments (DOE). The duration and temperature of the annealing process were selected as operational variables, and their initial range was chosen according to pre-study experiments, in which these two variables were delimited to focus the analysis within a reasonable interval. The presence (or absence) of a pressurized environment was also studied, but because RSM does not consider categorical factors, two identical DD experimental matrices were performed, one evaluating the presence of a pressurized environment and the other performed under normal atmospheric pressure conditions.

The number of experiences (N) in a DD is given by $N = k^2 + k + N_0$, where k is the number of optimized variables and N_0, the replicates at the central point. In the present case, no repetitions in the central point were made, providing a total of 7 experiences per design. Each test of the obtained design was repeated twice.

Five different responses related to the mechanical performance and the surface roughness of the evaluated material were measured, namely flexural modulus (E_{flex}), flexural strength (σ_{max}), strain at the flexural strength, average surface roughness (R_a), and average maximum peak-to-valley height of the roughness profile (R_z).

Analysis of the obtained results for this first phase using Minitab® Statistical Software was considered to discern between the most influential process parameters and identify the direction of the optimal zone. Besides, the presence of systematic errors was assessed by the randomness of the responses' residuals, and analysis of variance (ANOVA) was used to evaluate the significance of the models.

Based on these results, the experimental domain was moved, and a new DD experimental matrix was defined. The vicinity of the optimum was identified by a lack of fit of the adjusted second-order model (indicating a planar surface), whereas the optimum point and its prediction interval were determined using Minitab's response surface optimizer tool providing equal weights and importance to all responses to obtain an averaged optimum. Finally, confirmatory tests of the optimal point enabled the verification of the goodness of fit of the adjusted model.

2.2. Manufacturing of the test specimens

The three-point bending specimens used in this investigation were designed with a nominal thickness of 4 mm, a width of 10 mm, and 127 mm in length based on the ASTM D790 standard specifications [35].

Stratasys™ Insight software, and a Fortus 400mc professional fused deposition modeling printer from Stratasys™ were used to manufacture the samples using Ultem™ 9085 as the model material. This printer is provided with a thermal chamber that ensures a constant build temperature of 195 ℃ to enhance adhesion between the extruded material and the

already-deposited layer. All samples for the DD were fabricated in a single printing job using equal printing parameters, including a layer thickness of 0.254 mm, a ±45° raster angle, a solid part interior style, and one external contour. They were positioned in the printing bed in the upright direction (ZX orientation, see Fig. 1) and supported with a stabilizing wall for an enhanced finish. The choice of this printing orientation was motivated by the fact that parts printed in this direction tend to exhibit an inferior mechanical performance compared to other printing orientations due to inter-layer failure [9].

Additional specimens positioned laying flat (XY) and on the edge (XZ) on the printing bed were fabricated to test the outcome of the predicted optimal treatment conditions on different printing directions (Fig. 1).
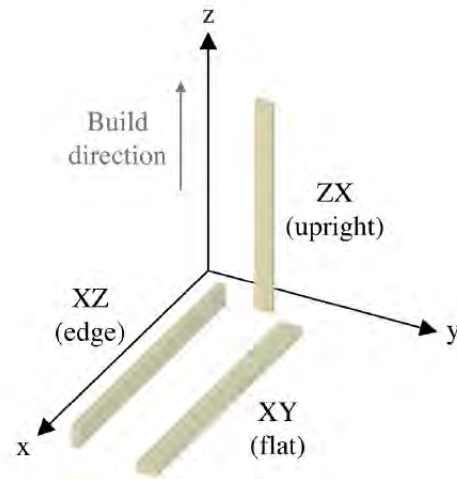

Figure 1: Schematic of the different printing orientations.

2.3. Thermal annealing and isostatic pressing

Thermal annealing treatments were performed in a TH2700 thermal chamber (Grip Engineering, Germany). Annealing of several PEI Ultem specimens was performed by firstly introducing them in a polyamide vacuum bag, equipped with a vacuum valve, and sealed with heat-resistant sealing tape to investigate the influence of vacuum conditions (emulating a pressurized environment at 0.9 bar) on the outcome of the thermal treatment, as depicted in Fig. 2. The vacuum pump used for this purpose was an RVP 21 single-stage rotary vane vacuum pump (Vuototecnica, Italy) with a pressurizing rate of $21 \, m^3 \, h^{-1}$. The remaining specimens were directly placed inside the chamber on a flat aluminum structure.

At the beginning of the annealing process, the treatment temperature was reached at a constant heating rate of 5 °C min^{-1}. Then, following the treatment time, specimens were left inside the chamber to slowly cool down using the chamber's ventilation system until ambient temperature conditions were reached.
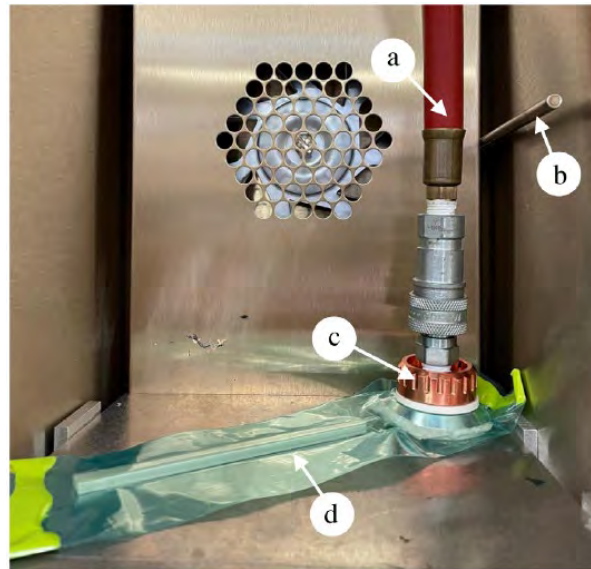
Figure 2: Experimental setup for the study of the influence of a pressurized environment on the outcome of the thermal annealing post-process. a) Connection to pump, b) Temperature sensor, c) Vacuum valve, d) PEI Ultem specimen inside a vacuum bag.

2.4. Surface roughness and dimensional accuracy

A Rugosurf 20 portable roughness gauge (TESA Technology, Switzerland) was used to assess changes in the average surface roughness (R_a) and the average maximum peak-to-valley height of the roughness profile (R_z) of the treated specimens. As shown in Fig. 3, surface roughness measurements were taken perpendicular to the layer deposition direction on the vertical face of each specimen before and after annealing. Measuring parameters were chosen according to the ISO 4288:1996 standard [36].

To address dimensional variations, measurements of the specimen's width, length, and height were recorded before and after the thermal treatments using a digital micrometer.

2.5. Mechanical testing

Three-point bending mechanical testing was performed in a Z030 universal testing machine (Zwick Roell, Germany) to evaluate the flexural modulus, flexural strength, and strain at flexural strength of both pristine and thermally treated samples. According to the ASTM D790 standard's recommendations (procedure A) [35] and considering a support span of 64 mm and the specimens' measurements stated in Section 2.2, a displacement rate of the testing machine's crosshead of 1.71 mm min^{-1} was fixed. Tests were conducted until rupture or a maximum stress value was reached, whichever occurred first.

Figure 3: Photograph of a ZX (printed upright) specimen showing the evaluated face and the direction of the surface roughness measurements (indicated by a white arrow).

2.6. *Microscope imaging*

A high-resolution Olympus DSX1000 digital microscope fitted with Olympus MPlanFL *N* 1x, 5x, and 20x objectives (Olympus Corporation, Japan) was used to capture three-dimensional surface and cross-sectional images of untreated and annealed samples. Cold mounting and refrigerated polishing were used to prepare cross-sectional samples to eliminate surface deformations due to heating or mechanical damage potentially caused by conventional cutting.

2.7. *X-ray diffraction and Raman spectroscopy*

X-ray diffraction (XRD) was conducted in a Panalytical Empyrean (Malvern Panalytical, Great Britain) diffractometer coupled with a PIXcel[3D] Medipix3 detector using a Cu K$_\alpha$ source in the Bragg-Brentano configuration. This technique was chosen to investigate changes in the underlying crystalline structure of PEI Ultem as a result of the thermal treatment.

Raman spectroscopy was employed to assess changes in the structure and chemical bonding of the thermally treated PEI Ultem specimens. Tests were conducted using a Thermo Scientific DXR2 Raman microscope (Thermo Fisher Scientific, USA) equipped with a 30 mW, 785 nm laser. Data acquisition in the range from 300 to 3300 cm^{-1} was done with a 10x objective, an aperture of 50 μm, and an exposure time of 30 s. The Raman spectra were processed through baseline correction to remove spectral contributions due to fluorescence.

3. Results and discussion

3.1. *Statistical analysis*

3.1.1. *First Doehlert Design*

The initial experimental domain is presented in Table 1. Additionally, the experimental matrix with the 28 experiments performed during the first DD is presented in Table 2 alongside the results for flexural modulus, flexural strength, strain at flexural strength, change in R_a, and change in R_z.

Table 1: Experimental domain for the first Doehlert Design.

Factor	Lower limit	Upper limit
Temperature [°C]	175	201
Time [h]	0.5	3.4
Pressure	Yes	No

Table 2: Experimental matrix and results for flexural modulus. flexural strength, strain at flexural strength, ΔR_a, and ΔR_z from the first Doehlert Design.

Sample ID	Run order	Time [h]	Temp [℃]	Pressure	Flexural modulus [MPa]	Flexural strength [MPa]	Strain at flexural strength [%]	ΔR_a [%]	ΔR_z [%]
1A	23	1.9	188	Yes	1948	77.6	4.0	-57.0	-47.2
1B	1	1.9	188	Yes	2012	78.3	3.9	-57.8	-45.9
2A	13	1.9	201	Yes	2271	107.2	5.7	-91.0	-87.6
2B	7	1.9	201	Yes	2340	107.9	5.6	-94.1	-90.0
3A	12	3.2	195	Yes	2274	95.4	4.3	-93.2	-91.0
3B	27	3.2	195	Yes	2225	101.1	4.8	-93.7	-90.7
4A	16	1.9	175	Yes	1848	62.6	3.3	-7.5	-8.5
4B	10	1.9	175	Yes	2007	63.5	3.4	-6.7	-10.0
5A	22	0.7	182	Yes	1960	65.0	3.5	-14.3	-13.1
5B	19	0.7	182	Yes	1784	68.8	3.6	-15.7	-15.2
6A	17	0.7	195	Yes	2205	81.9	3.8	-67.2	-56.0
6B	8	0.7	195	Yes	2414	87.7	4.2	-69.8	-57.2
7A	4	3.2	182	Yes	2187	71.6	3.7	-21.0	-21.2
7B	11	3.2	182	Yes	2120	66.7	3.4	-21.8	-19.3
8A	25	1.9	188	No	2004	69.1	3.8	0.4	-3.5
8B	2	1.9	188	No	1953	69.0	3.8	1.2	3.1
9A	20	1.9	201	No	1985	87.8	5.6	3.4	5.0
9B	9	1.9	201	No	1792	84.3	5.1	1.7	2.6
10A	18	1.9	175	No	1938	60.6	3.2	0.3	2.2
10B	5	1.9	175	No	1935	64.0	3.4	-1.5	0.5
11A	6	0.7	182	No	1949	63.7	3.4	0.0	0.5
11B	26	0.7	182	No	1899	65.7	3.5	-1.8	-2.3
12A	24	0.7	195	No	1901	69.6	3.8	0.8	0.9
12B	14	0.7	195	No	1868	66.5	3.8	0.6	3.8
13A	15	3.2	182	No	1897	65.3	3.5	0.8	1.7
13B	28	3.2	182	No	1942	63.1	3.4	0.3	1.8
14A	21	3.2	195	No	1869	81.5	5.2	-0.7	-1.1
14B	3	3.2	195	No	1946	75.4	4.4	1.4	4.4

Except in the case of strain at flexural strength, notable differences are observed between experiments performed in the presence of a pressurized environment (samples 1 to 7) and the ones conducted under normal atmospheric conditions (samples 8 to 14). Samples annealed in a pressurized environment present higher flexural modulus and flexural strength, and lower surface roughness. This indicates that, under the studied annealing conditions, the material has had enough time and temperature to flow and relocate itself within the intralayer and interlayer voids (that is, the specimens have experienced a densification) as denoted by a lower surface roughness and a higher mechanical resistance, respectively. The slow cooling is expected to have also contributed to the observed enhanced mechanical behavior by alleviating internal residual stresses that could have aroused during or after manufacturing.

ANOVA of the adjusted mathematical model for each response was examined given the non-heteroscedasticity or absence of systematic change in the spread of the residuals (as shown in Fig. 9 in the Appendix). Table 3 summarizes the main results for the ANOVA of each studied response: p-value of the lack-of-fit, p-value of the model, and R-squared (R^2). An extended version of the ANOVA can be consulted in the Appendix (Tables 7–11). Considering a significance level (α) of 0.05 (which indicates a 95% confidence on the null hypothesis testing), if the p-value of the lack-of-fit test is higher than α, it is safe to conclude that the predicted model accurately fits the data. That is the case of the three studied mechanical responses. In terms of surface roughness, the obtained low p-value does not necessarily imply a lack of fit of the model. This F-test considers the ratio between the lack-of-fit and the pure error and fails if the lack-of-fit is high or if the pure error (calculated with the replicates) is low, which happens in the case of the two surface roughness responses. In fact, model p-values for all responses lower than α and high R^2 denote that the adjusted models successfully explain the variance in all responses.

Three-dimensional representations of the response surfaces corresponding to each mathematical model, and average values for each pair of experimental points used to obtain these surfaces are displayed in Fig. 4. Two mathematical models were adjusted for each response, one corresponding to the experiments performed in a pressurized environment (black dots) and another for the experiments performed under normal atmospheric conditions (red dots). Light blue zones

indicate the best results, corresponding to stronger, more ductile samples with a decreased surface roughness. Coefficients of the adjusted full quadratic models are available in the Appendix (Table 12).

It should be noted that improvements in flexural strength and strain at flexural strength (Fig. 4(b) and (c)) follow a similar trend as they are highly influenced by the time and temperature of the process, and less dependent on the presence of a pressurized environment. The fact that annealed specimens can withstand higher external stresses (in this case, flexural loads) without cracks starting to propagate, leading to failure, is explained by a combination of released built-in thermal stresses and enhanced layer cohesion due to partial melting and solidification of interfilament unions.

Table 3: Analysis of variance for output responses in the first Doehlert Design.

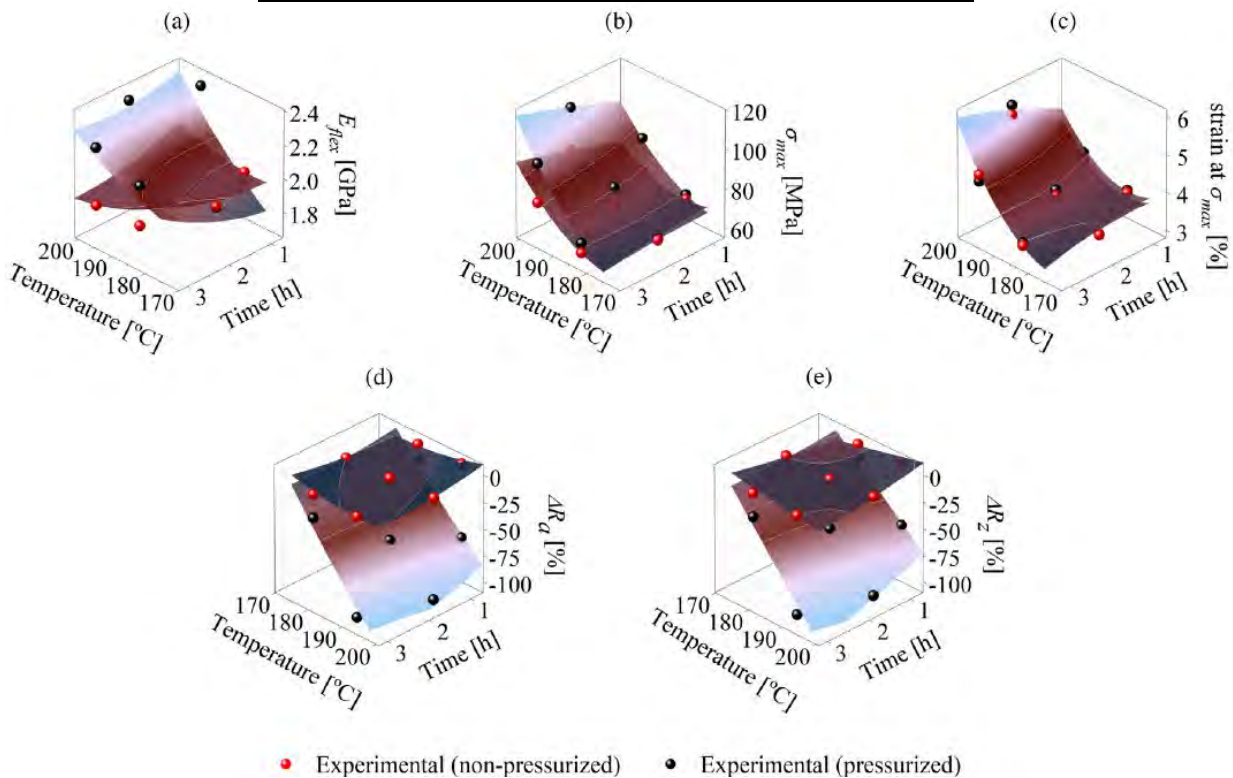| Response	p-value (Lack-of-fit)	p-value (Model)	R^2
Flexural modulus	0.052	0.000	77.95%
Flexural strength	0.710	0.000	97.81%
Strain at σ_{max}	0.296	0.000	92.58%
ΔR_a	0.000	0.000	98.04%
ΔR_z	0.000	0.000	97.96%

Figure 4: Response surfaces for flexural modulus (a), flexural strength (b), strain at flexural strength (c), ΔR_a (d), and ΔR_z (e) for the first Doehlert theoretical models. In each plot, one surface is adjusted to the red experimental dots (non-pressurized environment) and the other, to the black ones (pressurized environment).

As regards surface roughness and flexural modulus (Fig. 4(a), (d) and (e)), their tendencies are correlated. Under atmospheric pressure conditions, samples do not experience significant changes in these properties independently of the temperature and duration of the annealing. As explained in the improvements in flexural strength and strain at flexural strength, annealing reinforces the filament bonding, but despite the process being carried out over PEI Ultem's T_g, the material does not undergo a high enough decrease in its viscosity to start flowing and significantly change its shape or porosity (which has been reported to impact the properties of a material in its elastic region [37]). This explains the flatness of the adjusted response surfaces. However, in the cases where annealing is performed under a pressurized environment, the pressure exerted by the vacuum bag forces the relocation of material from the peaks to the valleys of the specimens' surfaces. Even though constant pressure is applied to the parts, the surface roughness decreases and the flexural

modulus increases with the increase in temperature and time as molecules have higher kinetic energy to move with respect to one another.

Neither of the adjusted surfaces presents an extremum within the studied range, indicating the need to move the new experimental domain towards the optimum response, situated at the higher end of the experimental domain (maximum mechanical properties and minimum surface roughness). For this purpose, Minitab optimizer tool was used, and results from the optimization are shown in Fig. 14 in Appendix. According to them, higher temperatures, higher annealing times, and a pressurized environment should be considered in the next step of the study.

3.1.2. *Second Doehlert Design and confirmatory experiments*

A graphical representation of the two Doehlert Designs is shown in Fig. 5, and the new experimental domain is summarized in Table 4.

The experimental matrix with the 14 experiments included in the second DD (all performed in a pressurized environment according to the first DD analysis) is presented in Table 6 together with the results for flexural modulus, flexural strength, strain at flexural strength, change in R_a, and change in R_z. Compared to the first DD, less pronounced changes in flexural modulus and surface roughness are observed, indicating a plateau in the improvement. However, the flexural strength and the strain at flexural strength suffered more remarkable changes, meaning that the increase in time of the treatment is beneficial in enabling a stronger and more ductile filament bonding. In other words, despite that samples may have densified and reduced their surface roughness to almost its maximum degree, the cohesion between filaments still has room for improvement.
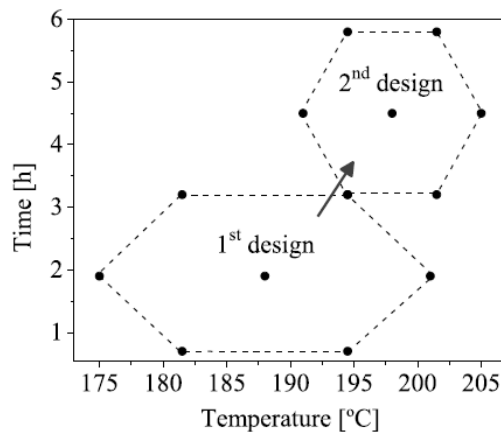

Figure 5: Graphical representation of the two Doehlert Designs. The arrow shows the direction of the movement of the experimental domain from the first to the second design.

Table 4: Experimental domain for the second Doehlert Design. All experiments were performed in a pressurized environment.

Factor	Lower limit	Upper limit
Temperature [°C]	191	205
Time [h]	3	6

Regarding the ANOVA, the results of which are presented in Table 5, interpretation of the p-value of the lack of fit indicates that the predicted model accurately fits the data for the mechanical properties. The obtained p-values of the surface roughness responses are not lower than the considered significance level, and thus the null hypothesis that the lack-of-fit is lower than the pure error cannot be rejected. This means that, as expected by the low curvature in the roughness responses (due to moderate surface roughness improvements observed during this first iteration) the quadratic model is not able to precisely fit the data. An extended version of the ANOVA can be consulted in the Appendix (Tables 13–17).

Table 5: Analysis of variance for output responses in the second Doehlert Design.

Response	p-value (Lack-of-fit)	p-value (Model)	R^2
Flexural modulus	0.126	0.213	53.36%
Flexural strength	0.817	0.000	93.89%
Strain at σ_{max}	0.176	0.000	95.30%
ΔR_a	0.011	0.340	45.05%
ΔR_z	0.000	0.090	64.15%

Table 6: Experimental matrix and results for flexural modulus, flexural strength, strain at flexural strength, ΔR_a, and ΔR_z from the second Doehlert Design

Sample ID	Run order	Time [h]	Temp [℃]	Pressure	Modulus	Flexural strength [MPa]	Flexural at flexural strength [MPa]	Strain ΔR_a [%] Strength [%]	ΔR_z [%]
15A	37	4.5	198		Yes	2374	112.9	6.5	-94.3
15B	36	4.5	198		Yes	2349	115.3	6.8	-94.2
16A	33	4.5	205		Yes	2155	118.5	7.9	-92.1
16B	39	4.5	205		Yes	2325	117.5	7.4	-93.2
17A	41	5.8	202		Yes	2316	117.2	7.5	-92.1
17B	29	5.8	202		Yes	2218	116.3	7.4	-91.4
18A	32	4.5	191		Yes	2264	97.8	4.6	-89.4
18B	30	4.5	191		Yes	2292	87.8	4.0	-90.1
3A	12	3.2	195		Yes	2274	95.4	4.3	-93.2
3B	27	3.2	195		Yes	2225	101.1	4.8	-93.7
19A	31	3.2	202		Yes	2376	114.4	6.6	-91.2
19B	35	3.2	202		Yes	2511	118.2	7.4	-92.4
20A	38	5.8	195		Yes	2282	108.5	5.6	-94.4
20B	34	5.8	195		Yes	2317	108.1	5.7	-91.4

On the other side, low R-squared values and high model p-values in flexural modulus and surface roughness indicate that the full-quadratic model is not capable of explaining variations in these responses. Observing the surface plots presented in Fig. 6(a), (d), and (e), one can notice a region with low response variations and an enclosed extremum.

Concerning flexural strength and strain at flexural strength, both models are able to explain the responses' variance, as determined by the non-significant model p-values and high R^2. Surface plots for these two cases (Fig. 6(b) and (c)) show that the maximum point is located at one end of the experimental domain. Nonetheless, Minitab's multiple response optimization results (Fig. 16 in the Appendix) suggest that the optimum point is found within the experimental domain (after 4.4 h of thermal annealing at 200.5 ºC). For this reason, no further iterations were made.

The obtained 95% prediction interval estimates that a sample annealed in the optimal conditions should have a flexural modulus of 2359±204 MPa, a flexural strength of 117.3±8.5 MPa, and a strain at maximum strength of 7.18±0.99%. In terms of surface roughness, the range of likely values for a single new optimal observation corresponds to a ΔR_a of 94±4%, and a ΔR_z of 92±9%.
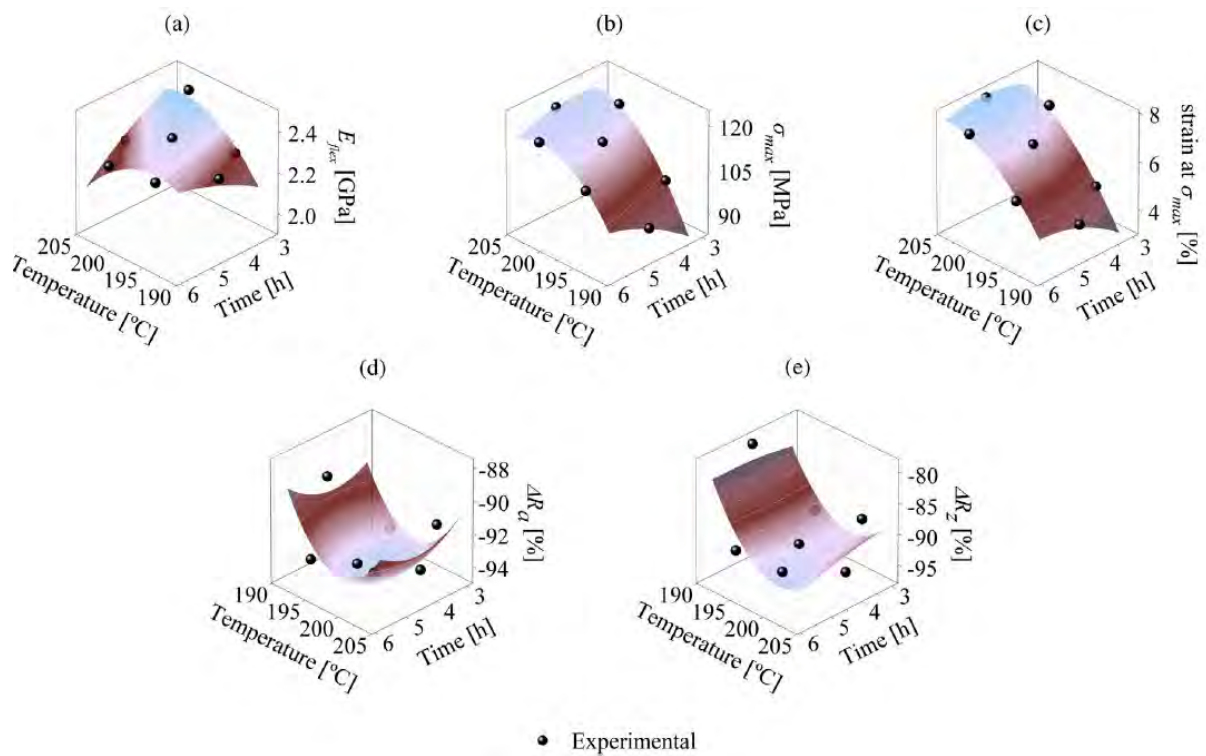
Figure 6: Surface plots for flexural modulus (a) flexural strength (b) strain at flexural strength (c) ΔR_a (d), and ΔR_z (e) for the second Doehlert theoretical model.

Confirmatory experiments' results obtained after treating six specimens with the optimal process conditions corroborated the adequacy of the optimizer's predictions, as all mechanical and surface properties fell within the predicted interval with a flexural modulus of 2310 ± 49 MPa, a flexural strength of 112 ± 2 MPa, a strain at flexural strength of $6.5\pm0.5\%$, a decrease in R_a of $93\pm1\%$, and a decrease of R_z of $91\pm1\%$.

3.2. Chemical and physical interpretation

Compared to untreated PEI Ultem specimens, samples annealed using the optimal process conditions showed significant improvements in surface roughness (higher than 90%) and their performance under flexural loads. More specifically, the flexural modulus increased, on average, by 21%, the flexural strength by 75%, and the strain at flexural strength by 83%. The following subsections will discuss the nature and reasoning behind these changes.

3.2.1. X-ray diffraction and Raman spectroscopy

XRD patterns shown in Fig. 7 are in line with PEI Ultem's XRD pattern reported by [24]. Results reveal PEI Ultem's non-crystalline structure in the form of a unique, broad hump in the 15 to 30 degrees 2theta range corresponding to a residual fraction mainly constituted by amorphous carbonaceous species. The fact that XRD patterns of untreated and annealed PEI Ultem samples are essentially equivalent implies that no changes in the material's amorphous nature were induced as a result of the thermal treatment.
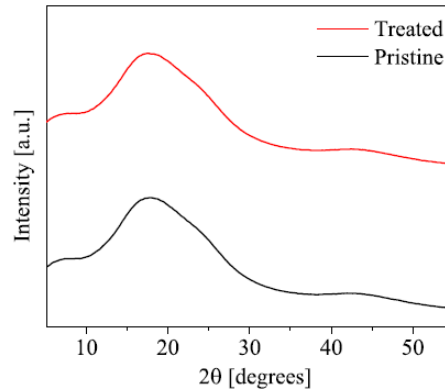
Figure 7: XRD patterns of annealed and pristine PEI Ultem specimens.

Concerning molecular composition and molecular structure, in Fig. 8, the obtained Raman spectra indicate no visible differences in the position or intensity of the peaks between the pristine and the annealed cases. This suggests that no degradation or changes in the molecular bonding have occurred at the surface level of the material.
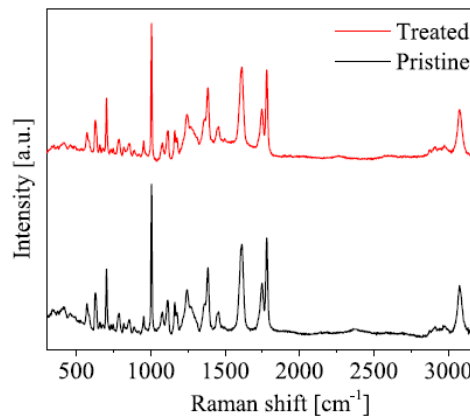

Figure 8: Raman spectra of annealed and pristine PEI Ultem specimens.

In the light of these results, it can be affirmed that the molecular integrity of PEI Ultem remains unaffected when subjected to the proposed thermal post-process. Therefore, changes observed in the mechanical performance are attributable solely to physical alterations such as filament bond reinforcement.

3.2.2. *Surface roughness and dimensional analysis*

Fig. 9 displays the surface roughness profile of pristine and thermally treated PEI Ultem specimens, where it can be seen that, in the pristine case, the outer filaments appear more rounded and have a total greater height (higher surface roughness) than in the thermally annealed specimen, whose surface is significantly flatter. Thermally treating the samples in a pressurized environment resulted in a decrease in surface roughness from $17.3\pm0.1\mu m$ to 1.2 ± 0.2 µm in R_a and from 70.4 ± 0.9 µm to $6.3\pm1.1\mu m$ in R_z.

Furthermore, even though the release of internal thermal stresses caused a significant increase in the length of the specimens annealed under atmospheric pressure conditions, isostatically pressurized and annealed specimens did not suffer geometrical distortions and changes in width and length were negligible or fell within the accuracy of the printer [38] (see Fig. .17 in the Appendix). In fact, samples compacted in height by an average $3.4\pm0.7\%$. This densification may well explain the enhanced mechanical properties of the post-processed samples, further discussed in the next section.
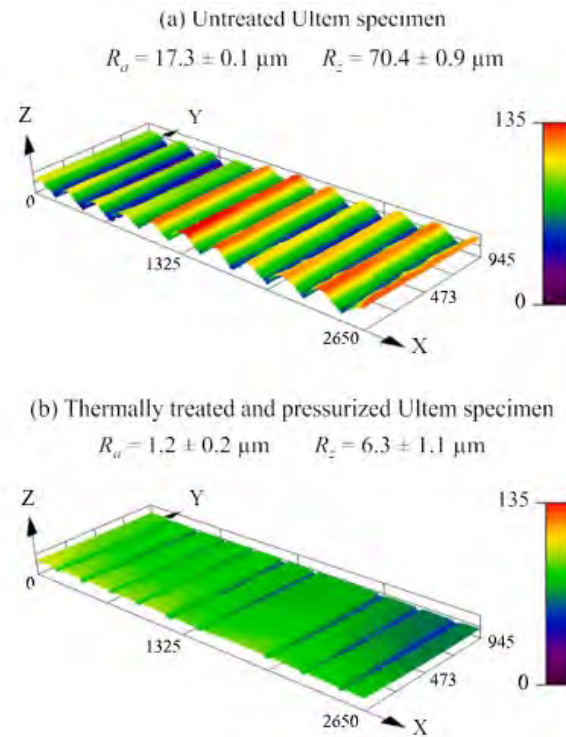
Figure 9: Representative 3D surface roughness profiles obtained by digital microscopy of pristine (a) and thermally annealed and pressurized (b) PEI Ultem samples.

3.2.3. *Mechanical performance*

With regards to the mechanical performance, Fig. 10 shows the results of the bending tests comparing stress-versus-strain curves of pristine (as-printed) and thermally annealed ZX (upright) PEI Ultem specimens. Compared to the pristine case, the six standard flexural PEI Ultem specimens treated with the optimum annealing conditions increased their stiffness, strength, and ductility. Because ZX specimens tend to mechanically fail due to interlayer separation, failure at higher strengths and higher strains means that there has been a significant improvement in the quality of the bonding between layers. Microscopy images of the fracture region of a pristine specimen (Fig. 10(a)) show a flat break region that indicates that failure has occurred due to layer separation. In contrast, images of an annealed sample in Fig. 10(b) reveal a more irregular break area, indicating that failure was not due to pure delamination. Furthermore, the interlayer filaments' cohesion has notably increased as the initial filament deposition path of the treated specimen is not as easily recognizable as in the case of the pristine specimen.
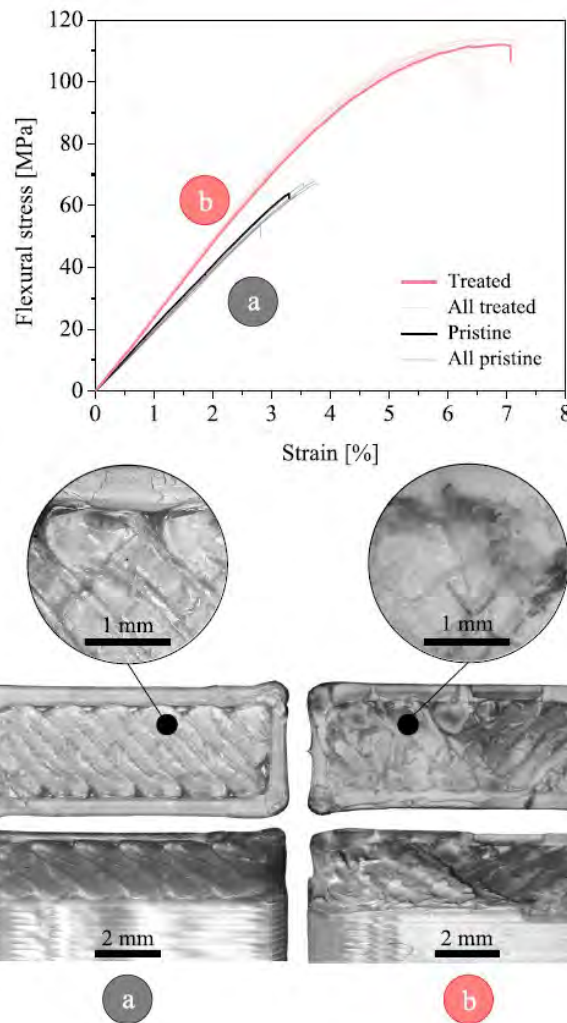
Figure 10: Flexural stress vs. strain curves and microscopy images of fracture region for pristine (a) and thermally annealed and pressurized (b) ZX PEI Ultem specimens.

3.2.4. *Effect on other printing configurations*

The optimal annealing conditions found for the ZX configuration were used to treat XY and XZ flexural specimens. As mentioned in the consulted literature [9], the mechanical properties of FDM PEI Ultem specimens are highly dependent on the orientation of the parts on the printing bed, and they are directly proportional to the percentage of the stress supported by the rasters. Because of the way XZ specimens are fabricated (with the outer-layer rasters completely perpendicular to the direction of the applied stress), the layer bonding has a minor influence on the mechanical properties, and thus this orientation presents the best performance under flexural stresses. Following an analogous reasoning, ZX specimens (whose outer-layer rasters are parallel to the direction of the applied stress) exhibit the poorest performance. The mechanical properties of XY specimens fall in the middle of the other two configurations due to the ±45° rasters disposition on their outer layer. Accordingly, the average flexural strength of pristine XZ (edge) specimens is 110±1 MPa, whereas it is 85±3 MPa for XY (flat) specimens and 64±5 MPa for ZX (upright) specimens.

Fig. 11 shows representative stress–strain curves for pristine and annealed samples fabricated using each of the studied printing orientations. From this comparative plot, one can observe an evident reduction in the anisotropy of the mechanical properties due to the thermal treatment in terms of the maximum stress that specimens can withstand, flexural modulus, and strain at flexural strength. For example, the maximum difference between the best- and the worst-performing specimens' flexural strength is reduced from 47 MPa (untreated) to 8 MPa (annealed), representing an 80% reduction in anisotropy.

Visual analysis of cross-sectional images of the samples, shown in Fig. 11, supports the findings regarding the mechanical properties: pristine samples, regardless of the printing orientation, are more porous (less dense) than their annealed counterparts. That is, when FDM PEI Ultem samples are annealed in a pressurized environment during the optimal time and temperature, specimens become denser and the unions of the part's rasters, reinforced.

4. Conclusions

The present study demonstrated the viability of post-processing FDM PEI Ultem parts via pressurized thermal annealing above the material's T_g followed by slow cooling to obtain specimens with enhanced mechanical behavior and surface quality.

Response surface methodology in the form of two consecutive Doehlert Designs was successfully used to identify the optimum treatment settings, which were found after 4.4 h of annealing in a pressurized environment at 200.5 °C. Using this combination of factors, PEI Ultem specimens compacted by 3% in height, reduced their surface roughness by more than 90%, and became 21% stiffer and 75% more resistant to bending stresses. Given that the chemical analysis via XRD and Raman spectroscopy indicated no changes in PEI Ultem's chemical and crystalline structure, the increased flexural modulus, flexural strength, and strain at flexural strength, and the decreased surface roughness, were attributed to partial melting, re-solidification, and bonding reinforcement.

In addition, post-processing of flexural specimens manufactured with different printing orientations (XY and XZ) using the aforementioned optimal annealing settings resulted in comparable improvements in the specimens' mechanical behavior and more uniform mechanical properties. In a nutshell, current findings evidence the suitability to thermally post-process FDM parts to minimize their mechanical anisotropy by reinforcing filament cohesion, which is one of the critical flaws of the fused filament 3D printing process.

Given the promising outcome of the herein presented work when thermal annealing is combined with isostatic compaction, future efforts should be directed towards exploring the effects of different pressure levels, scaling the process to geometries with a higher degree of complexity and infill percentages, and modeling and predicting the eventual deformations that the components might suffer as a consequence of the treatment validated in this study.
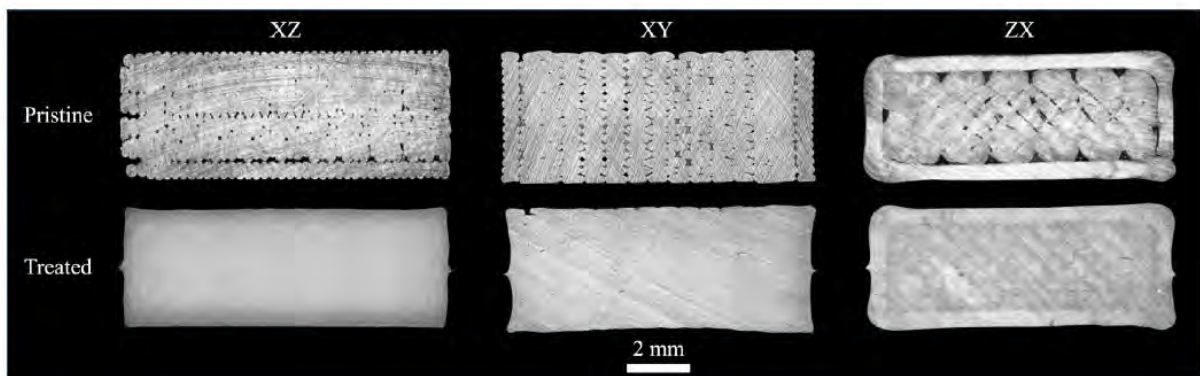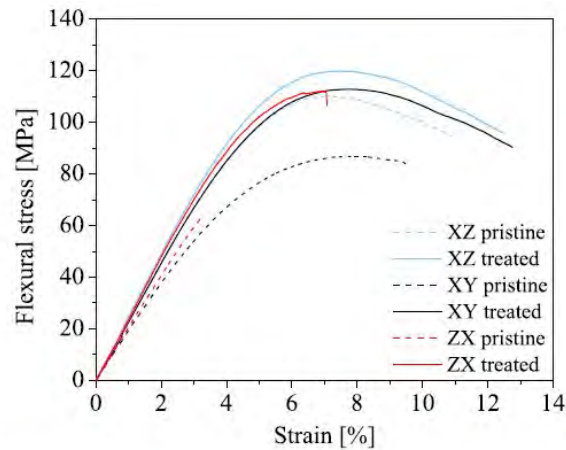

Figure 11: Stress-strain curves and cross-sectional images for different printing orientations.

CRediT authorship contribution statement

Ariadna Chueca de Bruijn: Methodology, Validation, Investigation, Writing - Original draft, **Giovanni Gómez-Gras:** Conceptualization, Investigation, Writing - review & editing, Formal analysis, **Laura Fernández-Ruano:** Response surface methodology, Validation, **Laia Farràs- Tasias:** Validation, Investigation, Writing - Original draft, **Marco A. Pérez:** Conceptualization, Investigation, Writing - review & editing, Funding acquisition.

Declaration of competing interest

The authors declare that they have no known competing financial interests or personal relationships that could have appeared to influence the work reported in this paper.

Data availability

The raw data required to reproduce these findings will be available to download from a data repository once the article is accepted for publication. Kindly cite this article, and the dataset, if utilizing or modifying the data in your work.

Acknowledgements

References

[1] S. Cailleaux, N. M. Sanchez-Ballester, Y. A. Gueche, B. Bataille, I. Soulairol, Fused Deposition Modeling (FDM), the new asset for the production of tailored medicines, J. Control. Release 330 (2021) 821–841. doi:10.1016/J.JCONREL.2020.10.056.

[2] C. Bellehumeur, L. Li, Q. Sun, P. Gu, Modeling of Bond Formation Between Polymer Filaments in the Fused Deposition Modeling Process, J. Manuf. Process. 6 (2004) 170–178. doi:10.1016/S1526-6125(04)70071-7.

[3] R. Lou, H. Li, J. Zhong, C. Zhang, D. Fang, A transient updated Lagrangian finite element formulation for bond formation in fused deposition modeling process, J. Mech. Phys. Solids 152 (2021) 104450. doi:10.1016/J.JMPS.2021.104450.

[4] P. Wang, B. Zou, S. Ding, Modeling of surface roughness based on heat transfer considering diffusion among deposition filaments for FDM 3D printing heat-resistant resin, Appl. Therm. Eng. 161 (2019) 114064. doi:10.1016/J.APPLTHERMALENG.2019.114064.

[5] N. G. Morales, T. J. Fleck, J. F. Rhoads, The effect of interlayer cooling on the mechanical properties of components printed via fused deposition, Addit. Manuf. 24 (2018) 243–248. doi:10.1016/J.ADDMA.2018.09.001.

[6] T. E. Shelton, Z. A. Willburn, C. R. Hartsfield, G. R. Cobb, J. T. Cerri, R. A. Kemnitz, Effects of thermal process parameters on mechanical interlayer strength for additively manufactured Ultem 9085, Polym. Test. 81 (2020) 106255. doi:10.1016/J.POLYMERTESTING.2019.106255.

[7] J. Kechagias, D. Chaidas, N. Vidakis, K. Salonitis, N. M. Vaxevanidis, Key parameters controlling surface quality and dimensional accuracy: a critical review of FFF process, Mater. Manuf. Process. 37 (2022) 963–984. doi:10.1080/10426914.2022.2032144.

[8] N. A. Fountas, I. Papantoniou, J. D. Kechagias, D. E. Manolakos, N. M. Vaxevanidis, Modeling and optimization of flexural properties of FDM-processed PET-G specimens using RSM and GWO algorithm, Eng. Fail. Anal. 138 (2022) 106340. doi:10.1016/J.ENGFAILANAL.2022.106340.

[9] A. Fore´s-Garriga, M. A. Pe´rez, G. Go´mez-Gras, G. Reyes-Pozo, Role of infill parameters on the mechanical performance and weight reduction of PEI Ultem processed by FFF, Mater. Des. 193 (2020) 108810. doi:10.1016/J.MATDES.2020.108810.

[10] J. S. Chohan, R. Singh, Pre and post processing techniques to improve surface characteristics of FDM parts: A state of art review and future applications, 2017. doi:10.1108/RPJ-05-2015-0059.

[11] A. Chueca de Bruijn, G. Go´mez-Gras, M. A. Pe´rez, A Comparative Analysis of Chemical, Thermal, and Mechanical Post-Process of Fused Filament Fabricated Polyetherimide Parts for Surface Quality Enhancement, Mater. 2021, Vol. 14, Page 5880 14 (2021) 5880. doi:10.3390/MA14195880.

[12] P. Sreejith, K. Kannan, K. R. Rajagopal, A thermodynamic framework for additive manufacturing, using amorphous polymers, capable of predicting residual stress, warpage and shrinkage, Int. J. Eng. Sci. 159 (2021) 103412. doi:10.1016/J.IJENGSCI.2020.103412.

[13] R. A. Wach, P. Wolszczak, A. Adamus-Wlodarczyk, Enhancement of Mechanical Properties of FDM-PLA Parts via Thermal Annealing, Macromol. Mater. Eng. 303 (2018) 1800169. doi:10.1002/MAME.201800169.

[14] K. Flu¨gel, R. Hennig, M. Thommes, Impact of structural relaxation on mechanical properties of amorphous polymers, Eur. J. Pharm. Biopharm. 154 (2020) 214–221. doi:10.1016/J.EJPB.2020.07.016.

[15] K. R. Hart, R. M. Dunn, J. M. Sietins, C. M. Hofmeister Mock, M. E. Mackay, E. D. Wetzel, Increased fracture toughness of additively manufactured amorphous thermoplastics via thermal annealing, Polymer (Guildf). 144 (2018) 192–204. doi:10.1016/J.POLYMER.2018.04.024.

[16] ULTEM 9085 Production-Grade Thermoplastic for Fortus 3D Printers, Technical Report, Stratasys, 2019. URL: https://www.stratasys.com/materials/search/ultem9085.

[17] J. Pisula, G. Budzik, P. Turek, M. Cieplak, An Analysis of Polymer Gear Wear in a Spur Gear Train Made Using FDM and FFF Methods Based on Tooth Surface Topography Assessment, Polymers (Basel). 13 (2021) 1649. doi:10.3390/POLYM13101649.

[18] S. Kim, H. Wu, A. Devega, M. Sico, W. Fahy, J. Misasi, T. Dickens, J. H. Koo, Development of polyether-imide composites for use as 3D printed thermal protection material, J. Mater. Sci. 55 (2020) 9396–9413. doi:10.1007/S10853-020-04676-6.

[19] A. Kafi, H. Wu, J. Langston, O. Atak, H. Kim, S. Kim, W. P. Fahy, R. Reber, J. Misasi, S. Bateman, J. H. Koo, Evaluation of additively manufactured ultraperformance polymers to use as thermal protection systems for spacecraft, J. Appl. Polym. Sci. 137 (2020) 49117. doi:10.1002/APP.49117.

[20] J. C. Najmon, S. Raeisi, A. Tovar, Review of additive manufacturing technologies and applications in the aerospace industry, Addit. Manuf. Aerosp. Ind. (2019) 7–31. doi:10.1016/B978-0-12-814062-8.00002-9.

[21] A. Chueca de Bruijn, G. Go´mez-Gras, M. A. Pe´rez, On the effect upon the surface finish and mechanical performance of ball burnishing process on fused filament fabricated parts, Addit. Manuf. 46 (2021) 102133. doi:10.1016/J.ADDMA.2021.102133.

[22] W. Seneviratne, J. Tomblin, B. Saathoff, Electroplating polymer based additive manufactured parts for enhanced structural performance, in: 36th Tech. Conf. Am. Soc. Compos. 2021 Compos. Ingen. Tak. Challenges Environ. ASC 2021, DEStech Publications, 2021, pp. 1859 – 1871. doi:10.12783/asc36/35881.

[23] T. D. McLouth, S. M. Gustafson, H. I. Kim, R. J. Zaldivar, Enhancement of FDM ULTEM® 9085 bond strength via atmospheric plasma treatment, J. Manuf. Process. 66 (2021) 179–188. doi:10.1016/J.JMAPRO.2021.04.021.

[24] E. Padovano, M. Galfione, P. Concialdi, G. Lucco, C. Badini, Mechanical and Thermal Behavior of Ultem® 9085 Fabricated by Fused-Deposition Modeling, Appl. Sci. 2020, Vol. 10, Page 3170 10 (2020) 3170. doi:10.3390/APP10093170.

[25] Y. Zhang, S. K. Moon, F. Baino, I. Hussainova, A. Riccio, The Effect of Annealing on Additive Manufactured ULTEM™ 9085 Mechanical Properties, Materials (Basel). 14 (2021) 2907. doi:10.3390/MA14112907.

[26] R. H. Myers, D. C. Montgomery, C. M. Anderson-Cook, Response Surface Methodology: Process and Product Optimization Using Designed Experiments, John Wiley & Sons, 2016, 2016.

[27] E. R. Fitzharris, I. Watt, D. W. Rosen, M. L. Shofner, Interlayer bonding improvement of material ex- trusion parts with polyphenylene sulfide using the Taguchi method, Addit. Manuf. 24 (2018) 287–297. doi:10.1016/J.ADDMA.2018.10.003.

[28] M. Hikmat, S. Rostam, Y. M. Ahmed, Investigation of tensile property-based Taguchi method of PLA parts fabricated by FDM 3D printing technology, Results Eng. 11 (2021) 100264. doi:10.1016/J.RINENG.2021.100264.

[29] J. D. Kechagias, S. P. Zaoutsos, D. Chaidas, N. Vidakis, Multi-parameter optimization of PLA/Coconut wood compound for Fused Filament Fabrication using Robust Design, Int. J. Adv. Manuf. Technol. 119 (2022) 4317–4328. doi:10.1007/S00170-022-08679-2.

[30] K. M. Agarwal, P. Shubham, D. Bhatia, P. Sharma, H. Vaid, R. Vajpeyi, Analyzing the Impact of Print Parameters on Dimensional Variation of ABS specimens printed using Fused Deposition Modelling (FDM), Sensors Int. 3 (2022) 100149. doi:10.1016/J.SINTL.2021.100149.

[31] J. D. Kechagias, N. Vidakis, Parametric optimization of material extrusion 3D printing process: an assessment of Box-Behnken vs. full-factorial experimental approach, Int. J. Adv. Manuf. Technol. 121 (2022) 3163–3172. doi:10.1007/S00170-022-09532-2.

[32] D. H. Doehlert, Uniform Shell Designs, Appl. Stat. 19 (1970) 231. doi:10.2307/2346327.

[33] J. M. Bosque-Sendra, M. Nechar, L. C. Rodr´ıguez, M. F. M. Molina, Optimization of analytical methods by using Doehlert's designs, Anal. Proc. Incl. Anal. Commun. 32 (1995) 375–377. doi:10.1039/AI9953200375.

[34] G. Ginoux, I. Vroman, S. Alix, Influence of fused filament fabrication parameters on tensile properties of poly-lactide/layered silicate nanocomposite using response surface methodology, J. Appl. Polym. Sci. 138 (2021). doi:10.1002/APP.50174.

[35] ASTM D790-17, Standard Test Methods for Flexural Properties of Unreinforced and Reinforced Plastics and Electrical Insulating Materials, ASTM Int. West Conshohocken, PA (2017). URL: https://www.astm.org/Standards/D790.

[36] ISO - ISO 4288:1996 - Geometrical Product Specifications (GPS) — Surface texture: Profile method — Rules and procedures for the assessment of surface texture, Technical Report, 1996. URL: https://www.iso.org/standard/2096.html.

[37] F. Bartolomeu, J. Fonseca, N. Peixinho, N. Alves, M. Gasik, F. S. Silva, G. Miranda, Predicting the output dimensions, porosity and elastic modulus of additive manufactured biomaterial structures targeting orthopedic implants, J. Mech. Behav. Biomed. Mater. 99 (2019) 104–117. doi:10.1016/J.JMBBM.2019.07.023.

[38] Stratasys, Fortus 400mc specification sheet, Technical Report, 2015. URL: https://www.stratasys.com/.

Appendix
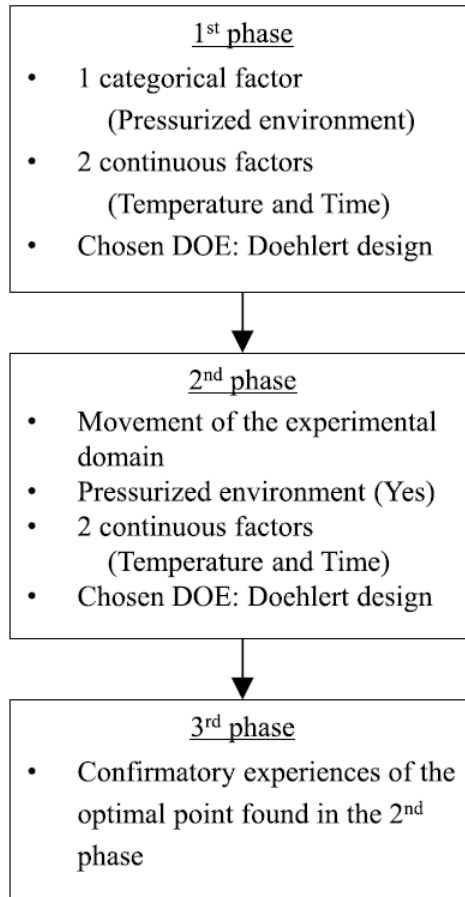
Figure .12: Schematic of the design of experiments' research methodology.
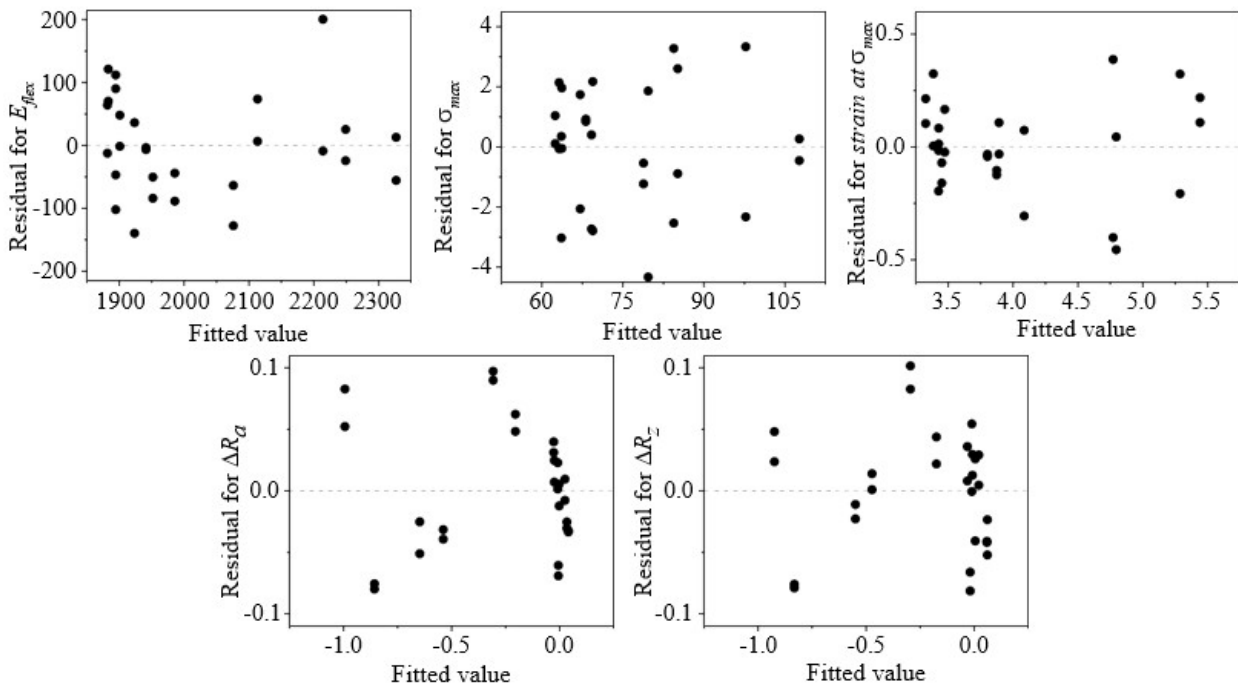
Figure .13: Residuals versus fits plots for the five output responses of the first Doehlert Design.

Table .7: Full ANOVA for the first Doehlert Design. The response is flexural modulus.

Source of variation	Degrees of freedom	Adjusted sums of squares	Adjusted mean squares	F-value	p-value
Model	8	601617	75202	8.39	0.000
Linear	3	384523	128174	14.31	0.000
Time	1	14333	14333	1.60	0.221
Temp	1	104311	104311	11.64	0.003
Pressure	1	265879	265879	29.68	0.000
Square	2	7051	3526	0.39	0.680
Time × Time	1	6887	6887	0.77	0.392
Temp × Temp	1	3222	3222	0.36	0.556
2-Way Interaction	3	207062	69021	7.70	0.001
Time × Temp	1	23930	23930	2.67	0.119
Time × Pressure	1	11003	11003	1.23	0.282
Temp × Pressure	1	172129	172129	19.21	0.000
Error	19	170212	8959		
Lack-of-Fit	5	86887	17377	2.92	0.052
Pure Error	14	83325			
Total	27	771829			

Table .8: Full ANOVA for the first Doehlert Design. The response is flexural strength.

Source of variation	Degrees of freedom	Adjusted sums of squares	Adjusted mean squares	F-value	p-value
Model	8	5061.54	632.69	106.12	0.000
Linear	3	4388.39	1462.8	245.36	0.000
Time	1	164.48	164.48	27.59	0.000
Temp	1	3418.29	3418.29	573.36	0.000
Pressure	1	805.63	805.63	135.13	0.000
Square	2	185.86	92.93	15.59	0.000
Time × Time	1	3.53	3.53	0.59	0.451
Temp × Temp	1	103.75	103.75	17.40	0.001
2-Way Interaction	3	548.31	182.77	30.66	0.000
Time × Temp	1	120.89	120.89	20.28	0.000
Time × Pressure	1	8.05	8.05	1.35	0.260
Temp × Pressure	1	419.37	419.37	70.34	0.000
Error	19	113.27	5.96		
Lack-of-Fit	5	19.63	3.93	0.59	0.710
Pure Error	14	93.65	6.69		
Total	27	5174.81			

Table .9: Full ANOVA for the first Doehlert Design. The response is strain at flexural strength.

Source of variation	Degrees of freedom	Adjusted sums of squares	Adjusted mean squares	F-value	p-value
Model	8	14.1841	1.7730	29.65	0.000
Linear	3	12.1833	4.0611	67.92	0.000
Time	1	0.6561	0.6561	10.97	0.004
Temp	1	11.4760	11.4760	191.94	0.000
Pressure	1	0.0512	0.0512	0.86	0.366
Square	2	1.5742	0.7871	13.16	0.000
Time × Time	1	0.0489	0.0489	0.82	0.377
Temp × Temp	1	0.8177	0.8177	13.68	0.002
2-Way Interaction	3	0.6845	0.2282	3.82	0.027
Time × Temp	1	0.6363	0.6363	10.64	0.004
Time × Pressure	1	0.0355	0.0355	0.59	0.450
Temp × Pressure	1	0.0127	0.0127	0.21	0.650
Error	19	1.1360	0.0598		
Lack-of-Fit	5	0.3722	0.0744	1.36	0.296
Pure Error	14	0.7638	0.0546		
Total	27	15.3201			

Table .10: Full ANOVA for the first Doehlert Design. The response is ΔRa.

Source of variation	Degrees of freedom	Adjusted sums of squares	Adjusted mean squares	F-value	p-value
Model	8	33718.2	4214.8	118.66	0.000
Linear	3	25743.2	8581.1	241.58	0.000
Time	1	229.6	229.6	6.46	0.020
Temp	1	7024.9	7024.9	197.77	0.000
Pressure	1	18488.7	18488.7	520.51	0.000
Square	2	49.0	24.5	0.69	0.514
Time × Time	1	36.2	36.2	1.02	0.326
Temp × Temp	1	39.9	39.9	1.12	0.302
2-Way Interaction	3	8085.5	2695.2	75.88	0.000
Time × Temp	1	114.3	114.3	3.22	0.089
Time × Pressure	1	259.0	259.0	7.29	0.014
Temp × Pressure	1	7712.2	7712.2	217.12	0.000
Error	19	674.9	35.5		
Lack-of-Fit	5	657.5	131.5	105.84	0.000
Pure Error	14	17.4	1.2		
Total	27	34393.1			

Table .11: Full ANOVA for the first Doehlert Design. The response is ΔR_z.

Source of variation	Degrees of freedom	Adjusted sums of squares	Adjusted mean squares	F-value	p-value
Model	8	29585.8	3698.2	114.16	0.000
Linear	3	22543.2	7514.4	231.96	0.000
Time	1	369.5	369.5	11.40	0.003
Temp	1	5915.9	5915.9	182.62	0.000
Pressure	1	16257.8	16257.8	501.85	0.000
Square	2	11.9	6.0	0.18	0.833
Time × Time	1	9.0	9.0	0.28	0.604
Temp × Temp	1	0.1	0.1	0.00	0.967
2-Way Interaction	3	7249.1	2416.4	74.59	0.000
Time × Temp	1	262.4	262.4	8.10	0.010
Time × Pressure	1	443.2	443.2	13.68	0.002
Temp × Pressure	1	6543.5	6543.5	201.99	0.000
Error	19	615.5	32.4		
Lack-of-Fit	5	555.8	111.2	26.05	0.000
Pure Error	14	59.7	4.3		
Total	27	30201.3			

Table .12: Coefficients of the theoretical model obtained in the first Doehlert Design in uncoded units.

Response	Pressure	Independent term	Time [h]	Temp [∘C]	Time [h] × Time [h]	Temp [∘C] × Temp [∘C]	Time [h] × Temp [∘C]
Flexural modulus	Yes	4527	844	-52	24.4	0.206	-4.76
Flexural strength	Yes	1169	-58.3	-12.78	-0.553	0.03691	0.3381
Strain at σ_{max}	Yes	113.6	-4.23	-1.202	-0.0651	0.003277	0.02453
ΔR_a	Yes	1370	48.7	-11.78	1.77	0.0229	-0.329
ΔR_z	Yes	478	82.2	-2.86	0.88	0.0009	-0.498
Flexural modulus	No	7878	802	-70	24.4	0.206	-4.76
Flexural strength	No	1332	-59.4	-13.69	-0.553	0.03691	0.3381
Strain at σ_{max}	No	114.3	-4.16	-1.207	-0.0651	0.003277	0.02453
ΔR_a	No	676	55.1	-7.88	1.77	0.0229	-0.329
ΔR_z	No	-165	90.6	0.73	0.88	0.0009	-0.498

Table .13: Full ANOVA for the second Doehlert Design. The response is flexural modulus.

Source of variation	Degrees of freedom	Adjusted sums of squares	Adjusted mean squares	F-value	p-value
Model	5	50494	10099	1.83	0.213
Linear	2	9185	4592	0.83	0.469
Time	1	7987	7987	1.45	0.263
Temp	1	1198	1198	0.22	0.654
Square	2	15572	7786	1.41	0.299
Time × Time	1	1007	1007	0.18	0.680
Temp × Temp	1	13919	13919	2.52	0.151
2-Way Interaction	1	25737	25737	4.67	0.063
Time × Temp	1	25737	25737	4.67	0.063
Error	8	44136	5517		
Lack-of-Fit	1	13291	13291	3.02	0.126
Pure Error	7	30845	4406		
Total	13	94630			

	Time [h]	Temperature [ºC]	Pressure
High	3.2	201.0	Yes
Optimum	3.2	201.0	Yes
Low	0.7	175.0	No

Composite desirability d = 1.000

Flexural modulus [MPa] y = 2453 d = 1.000

Flexural strength [MPa] y = 115.7 d = 1.0000

Strain at σ_{max} [MPa] y = 5.9 d = 1.0000

ΔR_a [%] y = -100 d = 1.0000
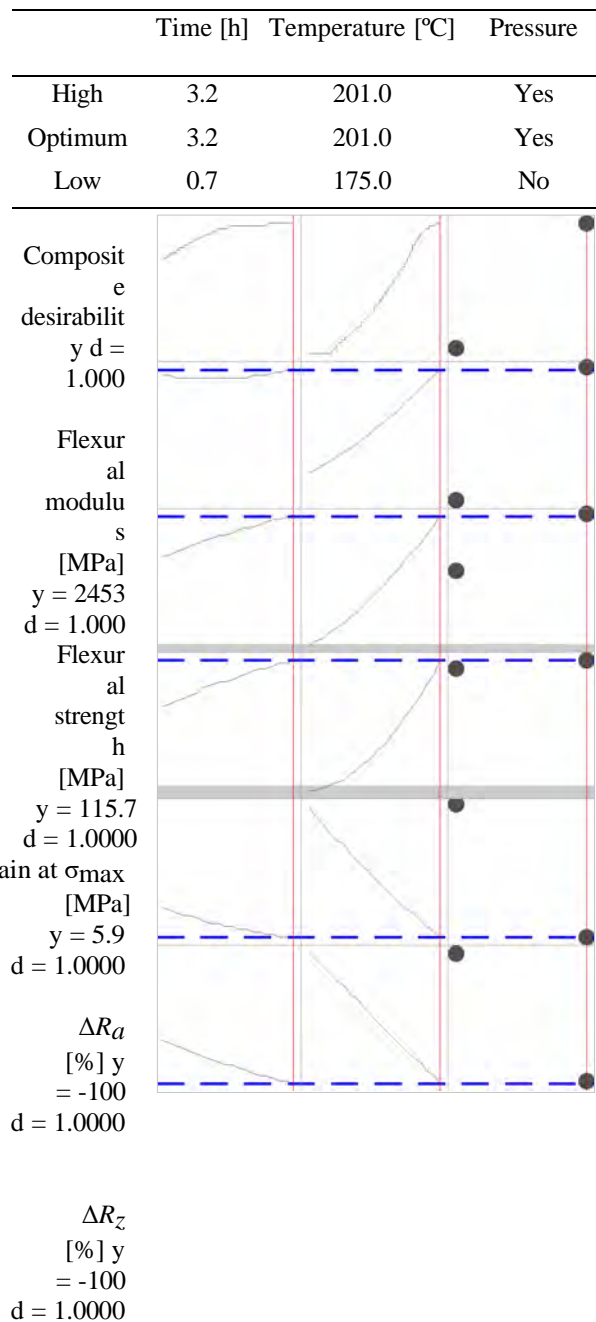
ΔR_z [%] y = -100 d = 1.0000

Figure .14: Results of the optimization from the first Doehlert Design. The weights and importance of all responses in the optimization process were fixed at 1.
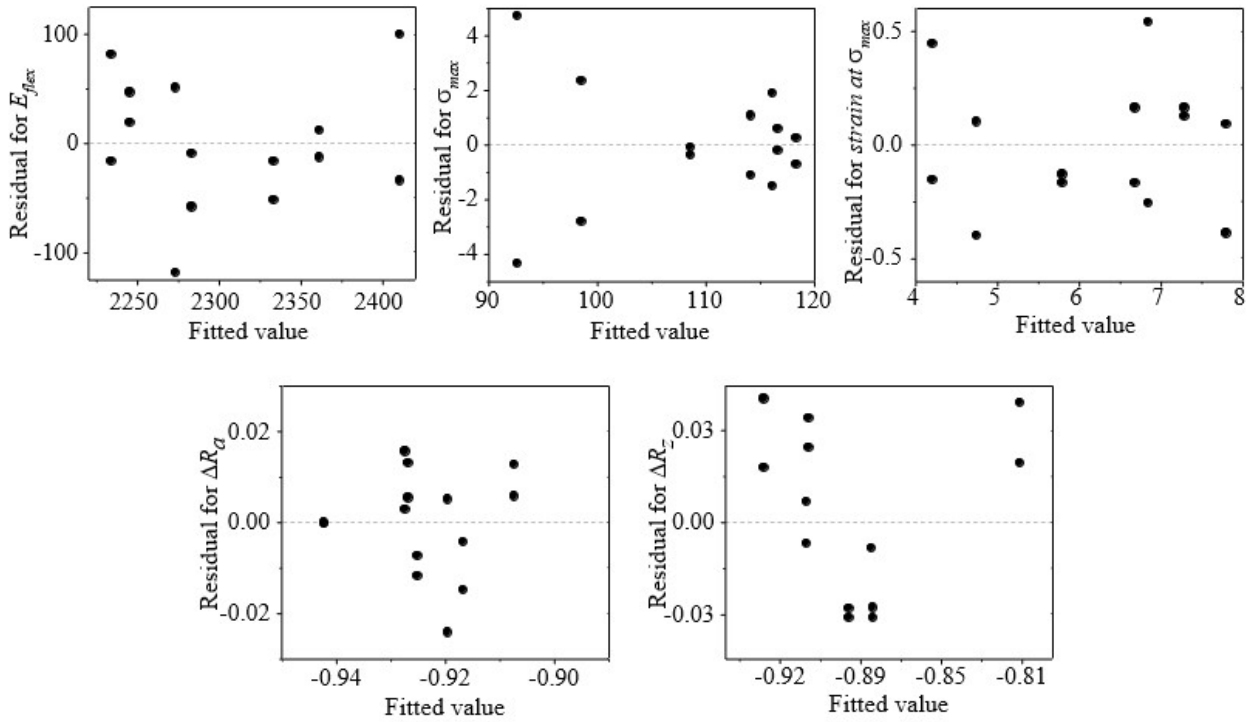
Figure .15: Residuals versus fits plots for the five output responses of the second Doehlert Design.

Table .14: Full ANOVA for the second Doehlert Design. The response is flexural strength.

Source of variation	Degrees of freedom	Adjusted sums of squares	Adjusted mean squares	F-value	p-value
Model	5	1194.86	238.973	24.57	0.000
Linear	2	1040.35	520.174	53.47	0.000
Time	1	55.39	55.388	5.69	0.044
Temp	1	984.96	984.961	101.25	0.000
Square	2	108.58	54.290	5.58	0.030
Time × Time	1	9.43	9.428	0.97	0.354
Temp × Temp	1	99.71	99.706	10.25	0.013
2-Way Interaction	1	45.94	45.936	4.72	0.062
Time × Temp	1	45.94	45.936	4.72	0.062
Error	8	77.82	9.728		
Lack-of-Fit	1	0.63	0.635	0.06	0.817
Pure Error	7	77.19	11.027		
Total	13	1272.69			

Table .15: Full ANOVA for the second Doehlert Design. The response is strain at flexural strength.

Source of variation	Degrees of freedom	Adjusted sums of squares	Adjusted mean squares	F-value	p-value
Model	5	21.4007	4.2801	32.47	0.000
Linear	2	20.5861	10.293	78.10	0.000
Time	1	1.1100	1.110	8.42	0.020
Temp	1	19.4760	19.476	147.77	0.000
Square	2	0.6285	0.3143	2.38	0.154
Time × Time	1	0.2781	0.2781	2.11	0.184
Temp × Temp	1	0.6165	0.6165	4.68	0.063
2-Way Interaction	1	0.1861	0.1861	1.41	0.269
Time × Temp	1	0.1861	0.1861	1.41	0.269
Error	8	1.0544	0.1318		
Lack-of-Fit	1	0.2581	0.2581	2.27	0.176
Pure Error	7	0.7962	0.1137		
Total	13	22.455			

Table .16: Full ANOVA for the second Doehlert Design. The response is ΔRa.

Source of variation	Degrees of freedom	Adjusted sums of squares	Adjusted mean squares	F-value	p-value
Model	5	141.7	28.3	1.34	0.340
Linear	2	15.5	7.8	0.37	0.705
Time	1	1.9	1.9	0.09	0.775
Temp	1	13.7	13.7	0.64	0.446
Square	2	124.9	62.5	2.94	0.110
Time × Time	1	24.0	24.0	1.13	0.318
Temp × Temp	1	122.6	122.6	5.78	0.043
2-Way Interaction	1	1.3	1.3	0.06	0.814
Time × Temp	1	1.3	1.3	0.06	0.814
Error	8	169.7	21.2		
Lack-of-Fit	1	106.6	106.6	11.82	0.011
Pure Error	7	63.1	9.0		
Total	13	311.4			

Table .17: Full ANOVA for the second Doehlert Design. The response is ΔRz.

Source of variation	Degrees of freedom	Adjusted sums of squares	Adjusted mean squares	F-value	p-value
Model	5	1714.3	342.9	2.86	0.090
Linear	2	950.6	475.3	3.97	0.063
Time	1	22.5	22.5	0.19	0.676
Temp	1	928.2	928.2	7.75	0.024
Square	2	743.6	371.8	3.11	0.100
Time × Time	1	4.6	4.6	0.04	0.850
Temp × Temp	1	458.6	458.6	3.83	0.086
2-Way Interaction	1	20.1	20.1	0.17	0.693
Time × Temp	1	20.1	20.1	0.17	0.693
Error	8	957.9	119.7		
Lack-of-Fit	1	836.6	836.6	48.26	0.000
Pure Error	7	121.4	17.3		
Total	13	2672.3			

Table .18: Coefficients of the theoretical model obtained in the second Doehlert Design in uncoded units.

Response	Independent term	Time [h]	Temp [℃]	Time [h] × Time [h]	Temp [℃] × Temp [℃]	Time [h] × Temp [℃]
Flexural modulus	46.1	0.237	-0.475	-0.0026	0.001197	-0.0011
Flexural strength	23.3	0.002	-0.245	0.00596	0.000619	-0.00028
Strain at σ_{max}	-91030	2554	884	-12.2	-2.09	-12.47
ΔR_a	-7669	116.9	74.1	-1.18	-0.1765	-0.527
ΔR_z	-624	8.75	5.9	-0.203	-0.01388	-0.0335

	Time [h]	Temperature [ºC]
High	5.8	205.0
Optimum	4.4	200.5
Low	3.2	191.0

Composite
desirability
d = 0.8018

Flexural modulus
[MPa] y = 2359
d = 0.57402

Flexural strength
[MPa]
y = 117.3
d = 0.92225

Strain at σ_{max}
[MPa]
y = 7.2
d = 0.81610

ΔR_a
[%] y = -94.06
d = 0.87958

ΔR_z
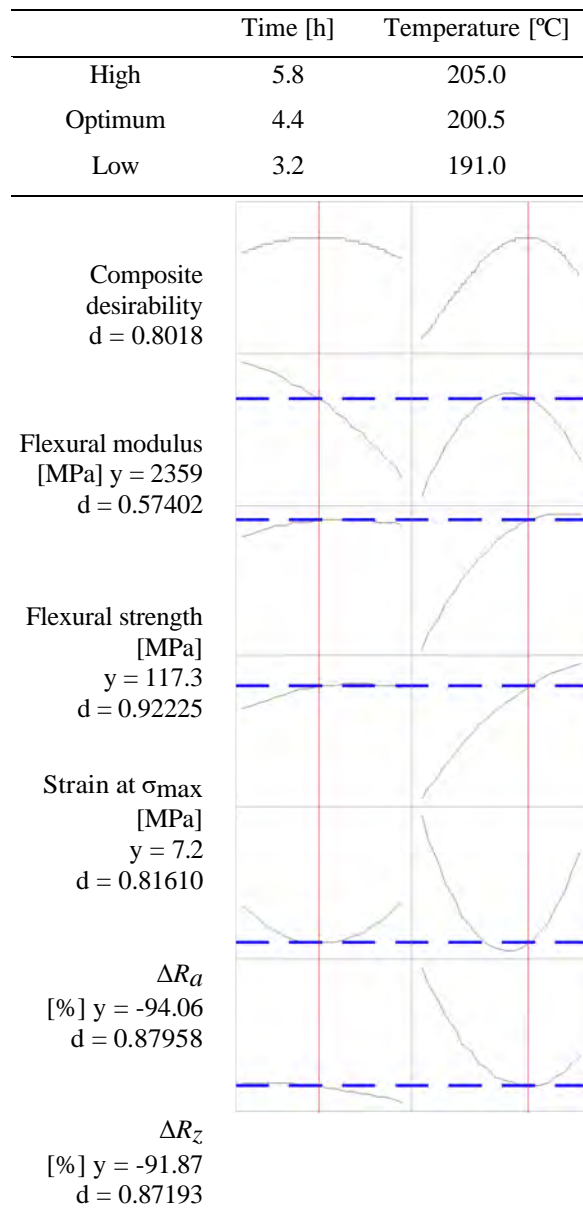[%] y = -91.87
d = 0.87193

Figure .16: Results of the optimization of the second Doehlert Design. The weights and importance of all responses in the optimization process were fixed at 1.
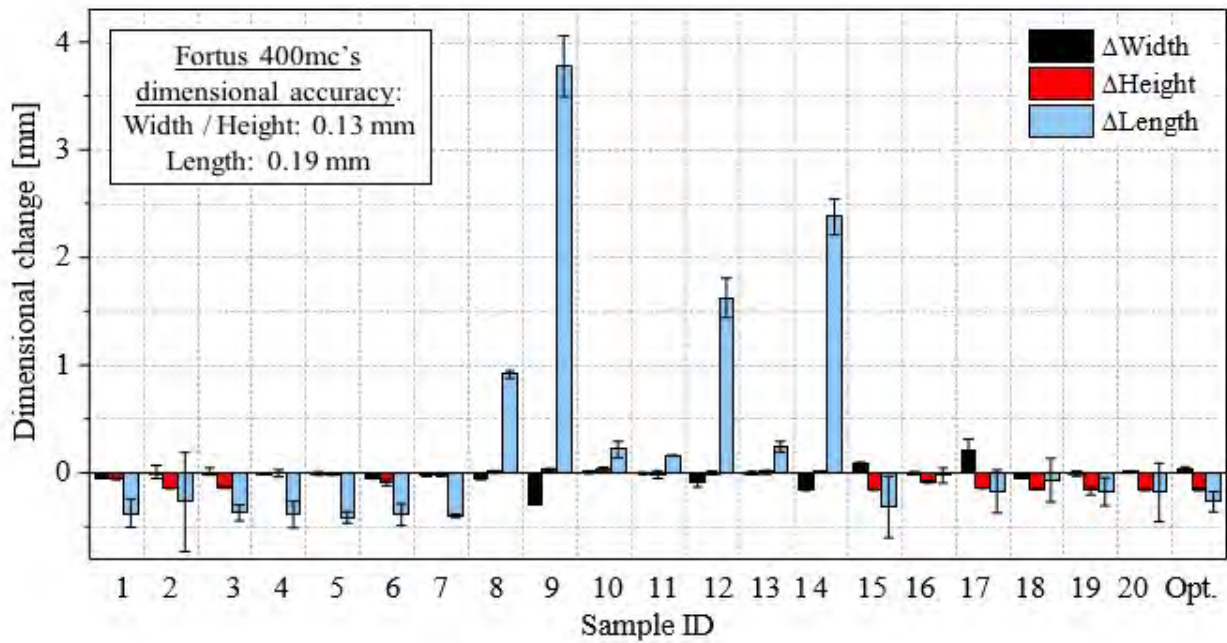
Figure .17: Average changes in width, height, and length of the thermally annealed specimens.